Published in IET Electric Power Applications
Received on 9th May 2014
Revised on 9th September 2014
Accepted on 25th September 2014
doi: 10.1049/iet-epa.2014.0168

ISSN 1751-8660

Integrated battery charger with power factor correction for electric-propulsion systems

Tian-Hua Liu, Yi Chen, Pei-Heng Yi, Jui-Ling Chen

Department of Electrical Engineering, National Taiwan University of Science and Technology, Taipei, Taiwan
E-mail: Liu@mail.ntust.edu.tw

Abstract: This paper proposes an on-board integrated battery charger for an electric-propulsion system. The system includes a rectifying diode bridge, an inverter, a permanent magnet motor, a digital signal processor, a battery set and three relays. By suitably controlling the three relays and the power switches of the inverter, the proposed system can be operated as either an electric-propulsion system or a battery charger. The integrated battery charger can be used to charge a 48 V battery set or a 192 V battery set from a single-phase 110 V_{rms} grid. The battery charger can be operated in a boost-converter charging mode or in buck-converter charging mode with input power factor higher than 0.9 when operating with 48 V battery or 192 V battery, which can meet the IEC 1000-3-2 standard. Only a diode bridge, an inductance-capacitance (LC) filter, and three additional relays are required in addition to the components for propulsion. The windings of the motor and the power switches of the inverter are shared for both the electric-propulsion system and the battery charger. A digital signal processor, TMS-320-F-2808, is used to execute all of the control algorithms. Experimental results validate the theoretical analysis and separately show the correctness and feasibility of the proposed method.

1 Introduction

The increase in gasoline prices and air pollution problems are prompting research on electric vehicles and plug-in hybrid electric vehicles [1–5]. The power of electric vehicles is supplied by batteries, which are usually charged through an AC source. Generally speaking, off-board chargers and the on-board charger require a reduction in its weight and volume since it is carried by the electric vehicle. In addition, the on-board battery charger usually charges the battery set for several hours. The input power source has to follow the international standards of near unitary power factor and low harmonic distortion to improve power quality of the AC source.

The integrated on-board charger is implemented by using the power conversion hardware of the electric vehicle with very few additional components to reduce its cost and volume. The charging system, therefore, shares many components with the propulsion system. To achieve this goal, several different integrated chargers have been proposed by researchers. The configurations of the integrated chargers can be divided into two major categories: the three-phase fast integrated charger and the single-phase integrated charger.

Three-phase fast integrated chargers are intended for commercial and public charging applications. Some researchers have proposed different topologies. For example, Khaligh and Dusmez [6] investigated the topological analysis of conductive and inductive charging methods for plug-in electric vehicles. In addition, a non-isolated, high-power, three-phase fast integrated charger was investigated by De Sousa *et al.* [7], Bruyere *et al.*[8] and Lacrox *et al.* [9] in Valeo Engine and Electrical Systems in 2010. This investigated non-isolated fast charger used three split windings of an AC motor, three H-bridge inverters and a DC/DC converter to fast charge the battery set.

On the other hand, several researchers have proposed single-phase integrated chargers. For example, Chang and Liaw [10] implemented an integrated battery charger for an electric vehicle with an input/output isolated characteristic. Solero [11] proposed a high-power factor boost-converter charger using the neutral point of a permanent magnet synchronous motor (PMSM). To implement a high-power and high-power factor buck-converter charger, Sousa *et al.* used a dual-motor and a dual-converter to achieve this goal. A completely integrated system, therefore, was achieved [12]. Yilmaz and Krein [13] proposed a two-stage charger, including a power factor correcting rectifier and a full-bridge DC/DC converter. This charger, however, required two-stage circuits and high-frequency inductances. Several researchers studied the integrated chargers with different configurations to reduce the weight, volume and cost of the whole circuit as well [14–18]. To improve the power factor of the AC source, an integrated charger with power factor correction is required. The input current has to track the input AC voltage well. Some researchers have investigated this issue. For example, Pellegrino *et al.* [19] proposed an integral battery charger with power factor correction for electric scooters.

For an integrated battery charger, the weight, size and cost are very important. To investigate the issue, in this paper, a new integrated battery charger with power factor correction is proposed. By using three relays, the propulsion system

and the charger can share the same power switches and the stator windings of the PMSM. The cost can be effectively reduced. In addition, the proposed method can be operated in two cases: in the first case, the battery set voltage is 192 V, higher than the maximum value of the input voltage. In the second case, the battery set voltage is 48 V, lower than the maximum value of the input voltage. The input current waveform can follow the input voltage wave form very well when the system is operated in the two different battery voltages mentioned above. As a result, the power factor and input current harmonics can meet the requirements of the IEC 1000-3-2 standard. To the authors' best knowledge, the idea proposed in this paper is new and has not been published in the previous papers.

This paper is organised as follows. First, a brief introduction is provided. Second, the details of the proposed system are described. Next, the basic operating modes of the proposed system are explained. Then, the implementation is discussed. After that, the experimental results are shown. Finally, some conclusions are given.

2 Proposed system

Fig. 1 shows the configuration of the main circuit of the proposed system. The main circuit consists of a rectifying bridge, an inverter, a PMSM and a battery set. When the system is operated in a propulsion mode, relay1 is turned on but relay2 and relay3 are turned off. Then, the system receives the power from the battery set directly and is totally disconnected from the single-phase AC voltage. By suitably changing the switching states of the inverter, the motor can be controlled. On the other hand, when the system is operated in charging mode, relay2 and relay3 are turned on but the relay1 is turned off. The rectifying bridge, therefore, can provide the DC voltage with 120 Hz pulsations. The inverter is separated into an 'H bridge' converter when connected to a 60 Hz grid because relay1 is turned off. The motor remains at a standstill without a mechanical brake and the torque is not produced during charging processes. As a result, the windings of the motor are operated as inductances of a buck converter or a boost converter. The power factor of the input AC source is not good enough when all relays are closed. To improve the power factor of the AC source, a new switching strategy is proposed in this paper. The switching strategies can be divided into two parts: the strategy for the boost-converter for 192 V battery and the strategy for the buck-converter for 48 V battery. By using the proposed switching strategies, the input power factor and input current harmonics can be effectively improved.

3 Basic operating modes of the system

There are three operating modes of the proposed system: propulsion mode, boost-converter charging mode and buck-converter charging mode. The details are described as follows. When relay1 is closed but relay2 and relay3 are opened, the proposed system is operated as a propulsion mode (Fig. 2).

3.1 Battery set charging method

The three-step charging method is used in this paper. The details are shown in Fig. 3. First, a constant-current charging mode is used from t_0 to t_1 to save the required charging time. Next, when the voltage of the battery set reaches its desired voltage, a constant-voltage charging mode is used to reduce the charging current. The constant-voltage charging time is from t_1 to t_2. Finally, the floating charging mode is used to slowly charge the battery set. The details of the floating charging mode are discussed in [20, 21]. By using the three-step charging modes, the battery life can be extended.

The NP 12-12 lead-acid batteries, which are manufactured by Yuasa Company, are used here. Each battery is rated 12 V and 12 Ah. The detailed specifications are shown as Table 1. When the buck-converter charging is operated, a series of four batteries is connected; on the other hand, when the boost-converter charging is operated, a series of 16 batteries is connected.

3.2 Boost-converter charging mode

One possibility is that the voltage of the battery set is higher than the maximum voltage of the input. In this situation, a boost-converter charging mode is required. The control algorithm of the boost-converter charging is shown in Fig. 4*a*. First, the open circuit battery set voltage V_0 is measured. If the capacity of the battery is below 83%, a constant-current charging mode is applied. The desired current command I_o^* is compared with the measured current I_o to determine the ΔI_o, i_g^*, Δi_g, v_{ic} and the switching states

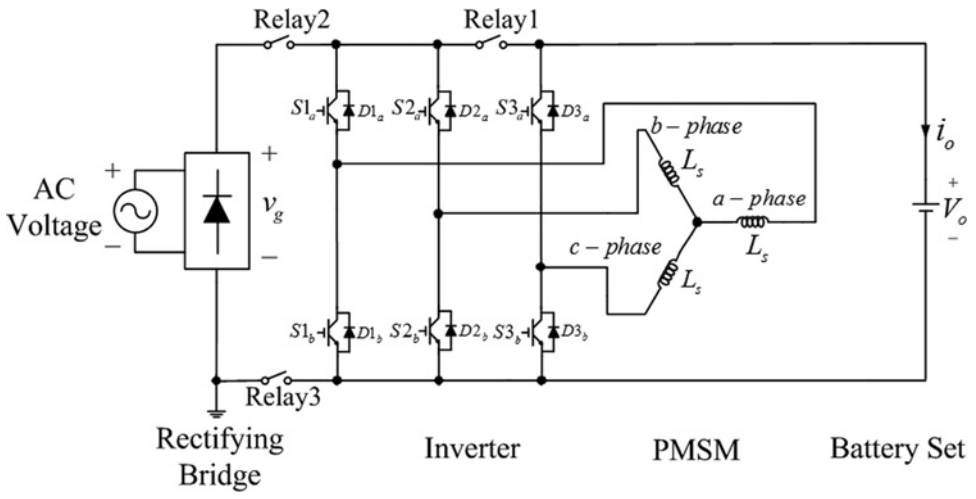

Fig. 1 *Configuration of the proposed system*

doi: 10.1049/iet-epa.2014.0168

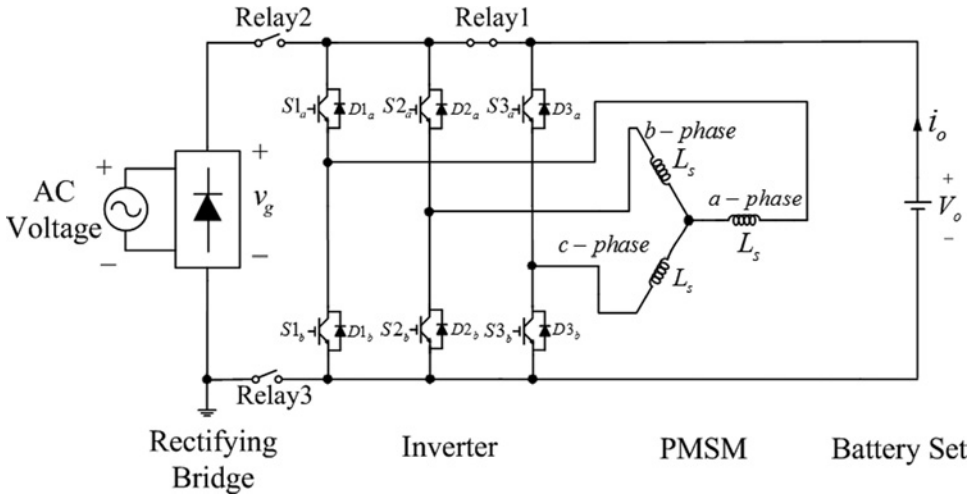

Fig. 2 *Configuration of propulsion mode*

of the insulated gate bipolar transistors (IGBTs). On the other hand, if the capacity of the battery is beyond 83%, a constant-voltage charging mode is used to calculate ΔV_o.

The output error signal ΔI_o or ΔV_o is processed by a proportional–integral (PI) controller and its output is multiplied by a unity signal, which is expressed as a $|\sin \omega t|$ in Fig. 4*a*, to obtain a desired current command i_g^*. The unity signal, $|\sin \omega t|$, is obtained by measuring the grid voltage, which is shown in Fig. 4*a*. After that, the desired current command i_g^* is compared with the real current i_g. The current error Δi_g is processed by a PI controller to obtain the control signal v_{ic}. It can be seen that the PI controller in the inner control loop processes the AC signal with frequency of 120 Hz. Therefore its integral part cannot effectively improve the AC component of the signal. In fact, the power factor control mainly relies on the proportional part of the controller. The power factor improves by selecting a higher proportional gain of the controller. The v_{ic} is subtracted from a triangular carrier, which has a modulation frequency of 10 kHz to generate the signal v_{error}. If v_{error} is ≥ 0, the $S3_b$ is turned on. On the other hand, if v_{error} is <0, $S3_b$ is turned off and the current flows through $D3_a$. $S1_a$ is kept on all the time.

Figs. 4*b* and *c* show the boost-converter charging circuits. From Fig. 4*b*, when $S1_a$ and $S3_b$ are turned on, the currents of the *a*-phase and *c*-phase inductances can be expressed as

$$\frac{d}{dt} i_g = \frac{1}{2L_s} v_g \tag{1}$$

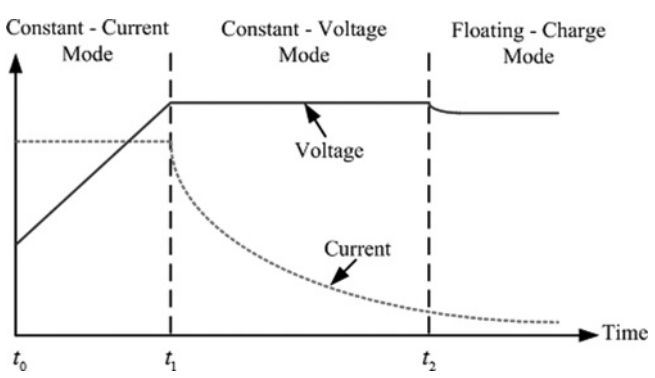

Fig. 3 *Three-step charging method*

where d/dt is the differential operator, i_g is the input current of the boost-converter, v_g is the input voltage of the boost-converter and L_s is the phase inductance of the motor. The current slope $(d/dt)i_g$ is positive because both the v_g and L_s are positive. As a result, the current i_g is increased when $S1_a$ and $S3_b$ are both turned on.

On the other hand, from Fig. 4*c*, when $S3_b$ is turned off, the currents of the *a*-phase and *c*-phase inductances can be expressed as

$$\frac{d}{dt} i_g = \frac{1}{2L_s}(v_g - V_o) \tag{2}$$

where V_o is the output voltage. The current slope $(d/dt)i_g$ is negative because the output voltage V_o is larger than the input voltage v_g. By suitably controlling $S3_b$, a current regulated controller can be achieved. Finally, the real current i_g can track the current command i_g^* well by using the proposed method.

3.3 Buck-converter charging mode

The second possibility is that the voltage of the battery set is smaller than the input voltage v_g. In this situation, a buck-converter charging mode is operated. The key principles are as follows. The buck-converter charging mode includes two boost modes and one interleaving buck-mode in one half-period of the grid voltage shown in Fig. 5*a*. For the boost-mode, the upper switch of the *a*-phase is on constantly, so that the *a*-phase is directly connected to the input voltage source. The *b*-phase is off and the *c*-phase is controlled as a single-phase boost converter. On the other hand, for the buck-mode, the *a*-phase and *b*-phase are controlled as a two-phase interleaved buck converter. The *c*-phase is on constantly. Therefore the *c*-phase is directly connected to the battery.

Table 1 Specification of NP 12-12 lead-acid battery

Rated voltage	Weight	Capacity	Maximum short circuit capability	Operating temperature
12 V	4.05 kg	12 Ah	360 A	−15 ~ 55°C

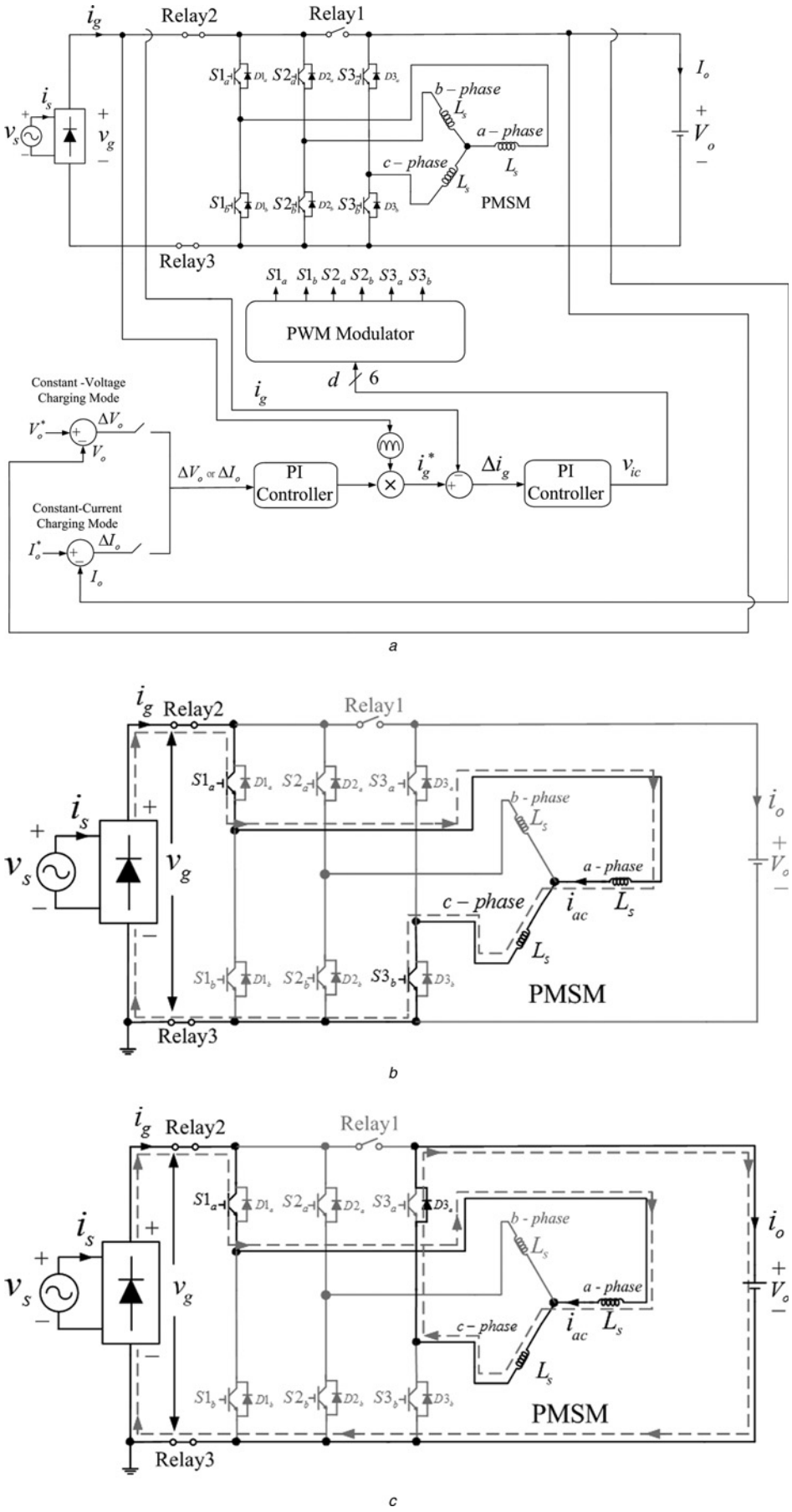

Fig. 4 *Boost-converter charging mode*

a Block diagram
b Main circuits for i_g increasing
c Main circuit for i_g decreasing

doi: 10.1049/iet-epa.2014.0168

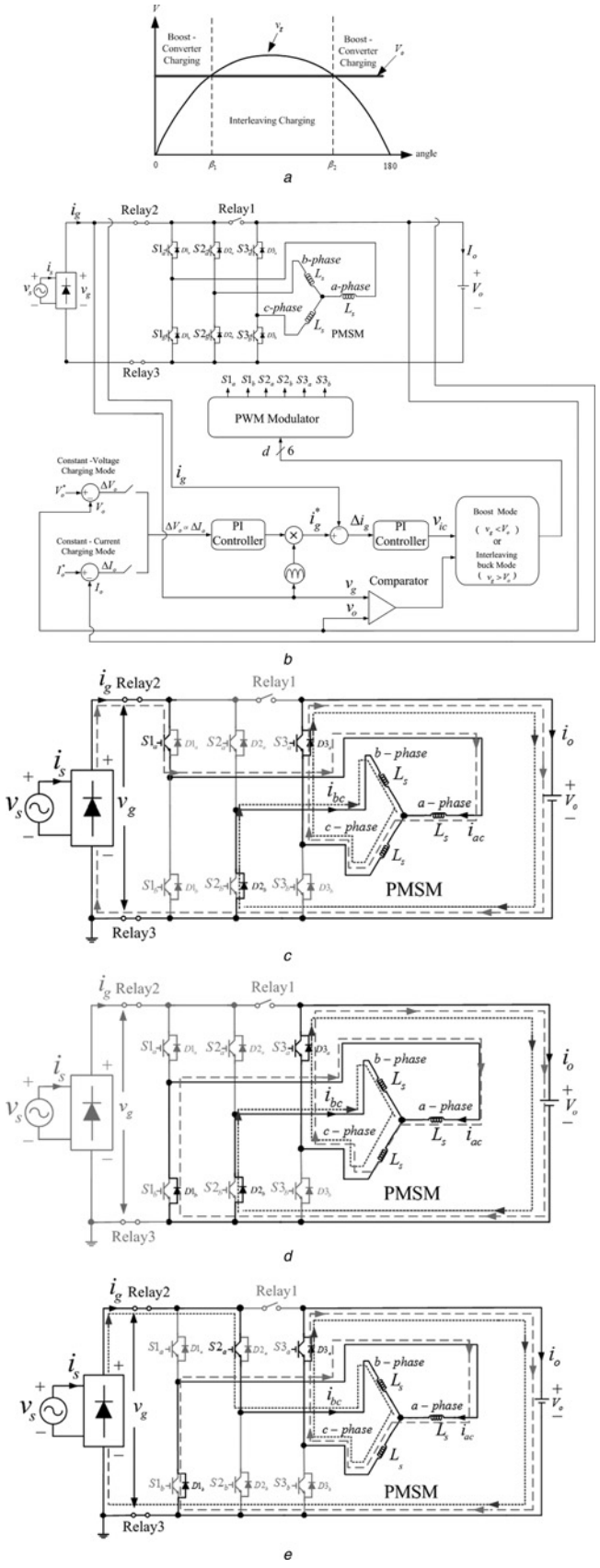

Fig. 5 *Buck-converter charging mode*

a Different charging modes
b Block diagram
c Interleaving charging for $i_g = i_{ac}$
d $S1_a$ and $S2_a$ are both turned off
e Interleaving charging for $i_g = i_{bc}$

Fig. 5*a* shows the operation method of the buck-converter charging mode. For the buck-converter charging mode, the input voltage is a half sinusoidal waveform and the output voltage is a DC voltage, which is lower than the maximum input voltage. According to Fig. 5*a*, from 0 degree to β_1 degree and β_2 degree to 180 degrees, the output voltage is higher than the input voltage. As a result, the boost-mode is used. By using the boost-mode, the input current waveform can easily be regulated to track the input voltage waveform as discussed in session C. On the other hand, from β_1 degree to β_2 degree, the input voltage is higher than the output voltage. Then, because of the opened circuit of relay1, the inverter is similar to an 'H' bridge. The inverter can be operated in interleaving buck-mode. By using the interleaving technique, the frequency of the input current ripple doubles. Therefore the input current between β_1 degree and β_2 degree can track the input voltage waveform well. By using the proposed two different modes shown in Fig. 5*a*, a current regulator is achieved.

The control algorithm of the buck-mode is shown in Fig. 5*b*. Fig. 5*b* is very similar to Fig. 4*a*. However, the switching patterns are different. First, the battery voltage is fed back when the charger is operated as a constant-voltage charge or a floating charge and the battery current is fed back when the charger is operated as a constant-current charge. Then, the voltage error ΔV_o or the current error ΔI_o is controlled by the PI controller. Next, the output of the PI controller is multiplied by a unity signal, $|\sin \omega t|$, to generate the current command, i_g^*. After that, the i_g^* is compared with i_g to obtain the current error, Δi_g. The Δi_g is controlled by a PI controller to generate the control signal v_{ic}. If $v_g < V_o$, the v_{ic} is modulated with a triangular modulation signal to determine the boost-mode switching states. On the other hand, if $v_g > V_o$, the v_{ic} is modulated with a triangular modulation signal to determine the buck-mode switching states. Finally, the switching states control the six power devices, $S1_a$, $S1_b$, $S2_a$, $S2_b$, $S3_a$ and $S3_b$ to charge the battery set. A closed-loop system is thus achieved.

The v_{error} signal is once again calculated as the subtraction of the triangular carrier from v_{ic}. When v_{error} is positive $S1_a$ is turned on, when it is negative $S1_a$ is turned off. The gating signals for $S2_a$ are calculated by delaying the signals for $S1_a$ by half of the switching period. The switch $S3_a$ is constantly held in conduction state. In this respect there can be four combinations of the states of the switches $S1_a$ and $S2_a$. The circuit analysis for each combination follows.

First, Fig. 5*c* shows the buck-converter charging circuit for $i_g = i_{ac}$. In this time interval, $S1_a$ is turned on and $S2_a$ is turned off. The current i_g can be expressed as

$$\frac{d}{dt} i_g = \frac{d}{dt} i_{ac} = \frac{1}{2L_s}(v_g - V_o) \tag{3}$$

At the same time, $D2_b$ is conducting. The current i_{bc} can be expressed as

$$\frac{d}{dt} i_{bc} = \frac{1}{2L_s}(-V_o) \tag{4}$$

Therefore i_g and i_{ac} are increasing and i_{bc} is decreasing. Next, Fig. 5*d* shows $S1_a$ and $S2_a$ are both turned off, which is the free-wheeling interval. In this interval, i_g is zero and i_{bc} and i_{ac} are decreased.

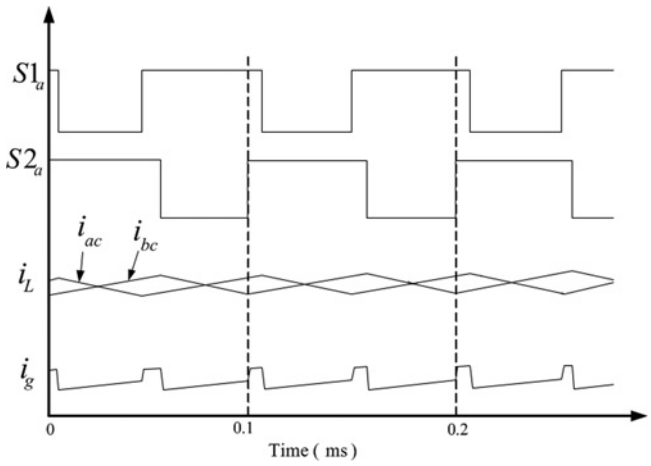

Fig. 6 *Waveforms of switching states and input current*

After that, Fig. 5*e* shows the buck-converter charging circuit for $i_g = i_{bc}$. The switches $S2_a$ is turned on and $S1_a$ is turned off. Then, the current i_g can be expressed as

$$\frac{d}{dt} i_g = \frac{d}{dt} i_{bc} = \frac{1}{2L_s}(v_g - V_o) \tag{5}$$

At the same time, because $D1_b$ is conducting, the current i_{ac} can be expressed as

$$\frac{d}{dt} i_{ac} = \frac{1}{2L_s}(-V_o) \tag{6}$$

Therefore i_g and i_{bc} are increasing and i_{ac} is decreasing. Finally, $S1_a$ and $S2_a$ are both turned off again, which is the free-wheeling interval. In this interval, i_g is zero and i_{bc} and i_{ac} are decreased. When the duty ratio of $S1_a$ and $S2_a$ is larger than 50%. There is a period when both switches are conducting. The situation is discussed in Fig. 6.

Fig. 6 shows the waveforms of the switches $S1_a$, $S2_a$ and the current i_L, i_g when the interleaving duty is equal to 0.6. As you can observe, the input current ripple of the current i_g can be effectively improved because of using the proposed interleaving method with the doubling of the switching frequency.

4 Implementation and experimental results

The implemented system is shown in Fig. 7. Fig. 7*a* shows the control block diagram of the implemented system. The system includes the hardware circuit and the software program, which is executed by the digital signal processor (DSP), TMS-320-F-2808. First, the DSP reads the voltage v_g, current i_g, output voltage V_o and output current i_o. Next, the DSP executes the control algorithms to determine the switching states of the inverter and relay1, relay2 and relay3. Finally, the system can achieve the propulsion control, boost-converter charging mode or buck-converter charging mode and then improve the input power factor as well.

Fig. 7*b* shows the layout of the switching loop, which includes the relay module with three relays, and the inverter module with three IGBT packages inside. In fact, the proposed schematic cannot be implemented by using the 6-pack three-phase IGBT. The IGBTs used in this paper were made by Mitsubishi Company. The IGBT has rated voltage 600 V, rated current 200A, rise time 240 ns, falling time 420 ns and operating temperature from −40 to 150°C.

Owing to the budget limitation of the project, the electric vehicle (EV) system has not been connected to the proposed electric-propulsion system; as a result, the EV load has not been investigated. It will be studied in the near future.

Fig. 7*c* shows the photograph of the implemented control circuit, which includes the power stage of the inverter, gate driver, relays, voltage sensing circuit, current sensing circuit and DSP. The sampling interval of the current control is 100 μs and the sampling interval of the voltage control is

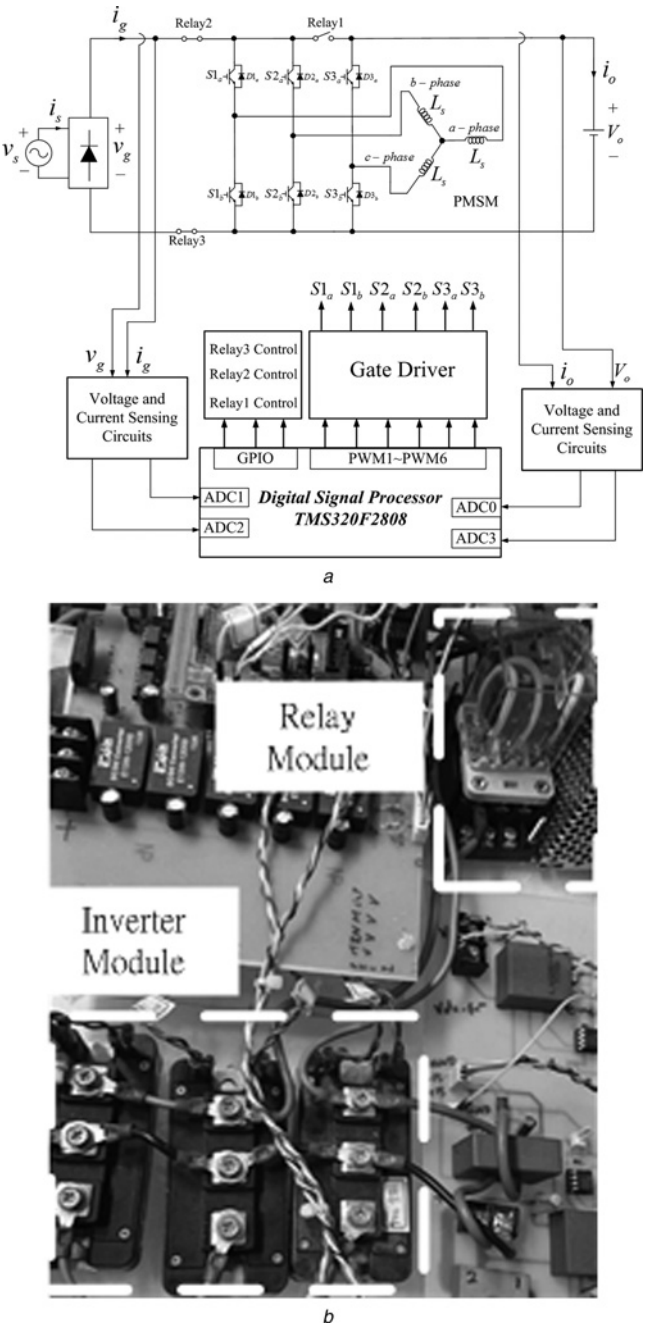

Fig. 7 *Proposed system*

a Block diagram
b Layout of the relay and power circuit
c Implemented control circuit
d Whole system

doi: 10.1049/iet-epa.2014.0168

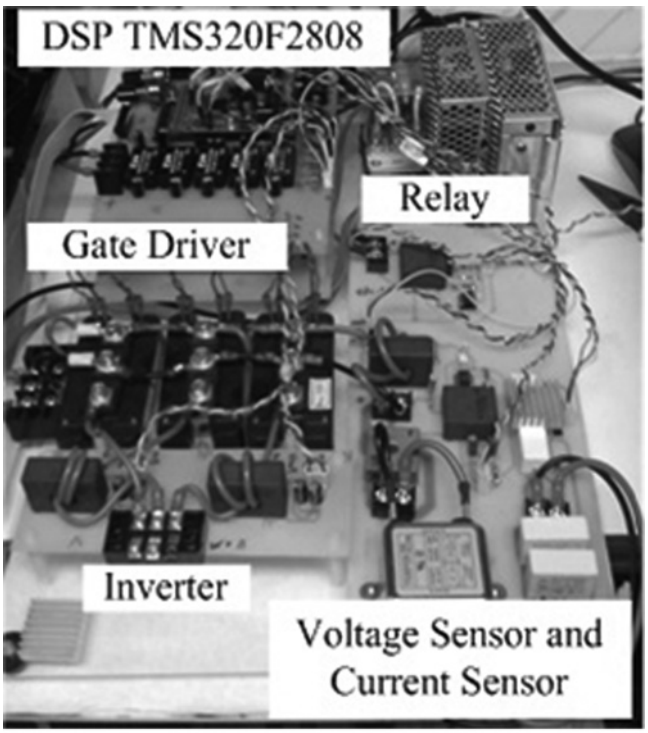

d

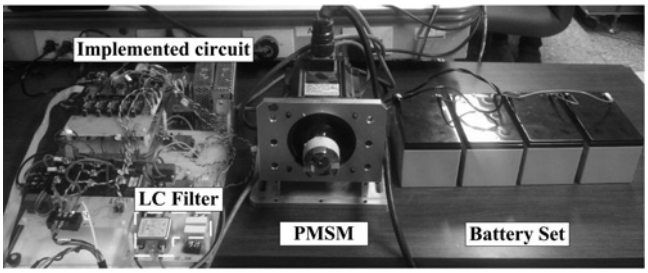

e

Fig. 7 *Continued*

1 ms. As you can observe, the whole circuit is very simple because most important jobs are executed by the DSP. Compared with the traditional electric-propulsion drive, a diode bridge, an LC filter near the AC source, and three extra relays are added here. Fig. 7*d* shows the whole system, including the PMSM, the implemented circuit and the battery set, which includes either four or twelve lead-acid batteries.

After the battery is fully charged, it becomes 13.52 V. In this paper, a four series battery is used for the buck-converter charging and a twelve series battery is used for the boost-converter charging. The PMSM motor was made by Ray Electrical Manufacture and Assembly Company. It is a three-phase, 220 V, 9.6 A, 2 kW, eight pole, rated speed 2000 r/min, surface-mounted PMSM. The stator resistance is 0.36 Ω, and the stator inductance is 2.8 mH. The inertia is 13.43 kg cm^2 and the viscous friction is 0.00028 Nm s/rad. An LC filter is used near the AC source to reduce the current harmonics of the input side. The inductance is 0.5 mH and the capacitance is 0.47 μF. The grid voltage is a single-phase, 110 V_{rms} and 60 Hz AC source. The PI controllers are designed by using pole-placement method. However, because of the scope and page limitations of this paper, the detailed descriptions are omitted here.

Several experimental results are discussed here to validate theoretical analysis. Fig. 8 shows the measured input voltage and current waveforms using the boost-converter charging mode. Fig. 8*a* is the measured input voltage and current waveform for the constant-current charging. The measured power factor of Fig. 8*a* is 0.97. Fig. 8*b* is the measured input voltage and current waveforms using the constant-voltage charging. The measured power factor of Fig. 8*b* is 0.94. According to Figs. 8*a* and *b*, the current waveforms can track the voltage waveform well. The measured input current waveforms are varied at different charging powers. The major reason is that the zero-crossing distortion interval is reduced at a larger charging power. In general, this can be improved by more complex control algorithm, which will be studied by the authors in the future. Fig. 9 shows the measured waveforms of the buck-converter charging mode. Fig. 9*a* is the measured waveforms using the constant-current charging with interleave. The measured power factor of Fig. 9*a* is 0.95. Fig. 9*b* is the measured waveforms using the constant-voltage charging with interleave. The measured power factor of Fig. 9*b* is 0.92. Fig. 9*c* shows the detailed switching states of $S1_a$ and $S2_a$, and the current waveforms of i_{bc}, i_{ac} and i_g. Fig. 9*d* is the measured waveforms using the constant-current charging without interleave. There is a discontinuity between the boost and buck operations and

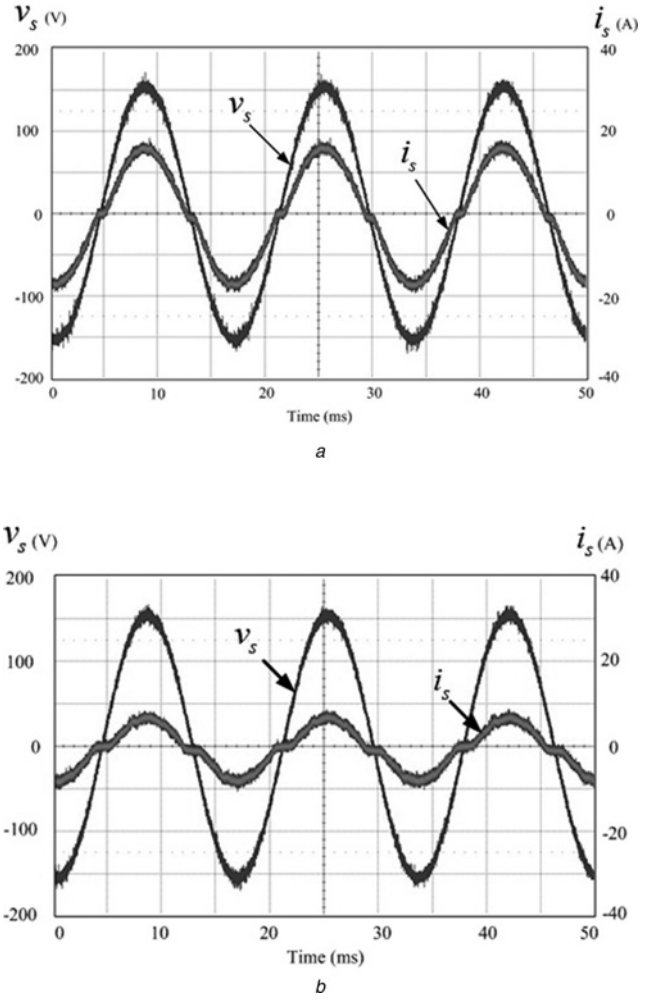

Fig. 8 *Measured input waveforms of boost-converter charging*

a Constant current
b Constant voltage

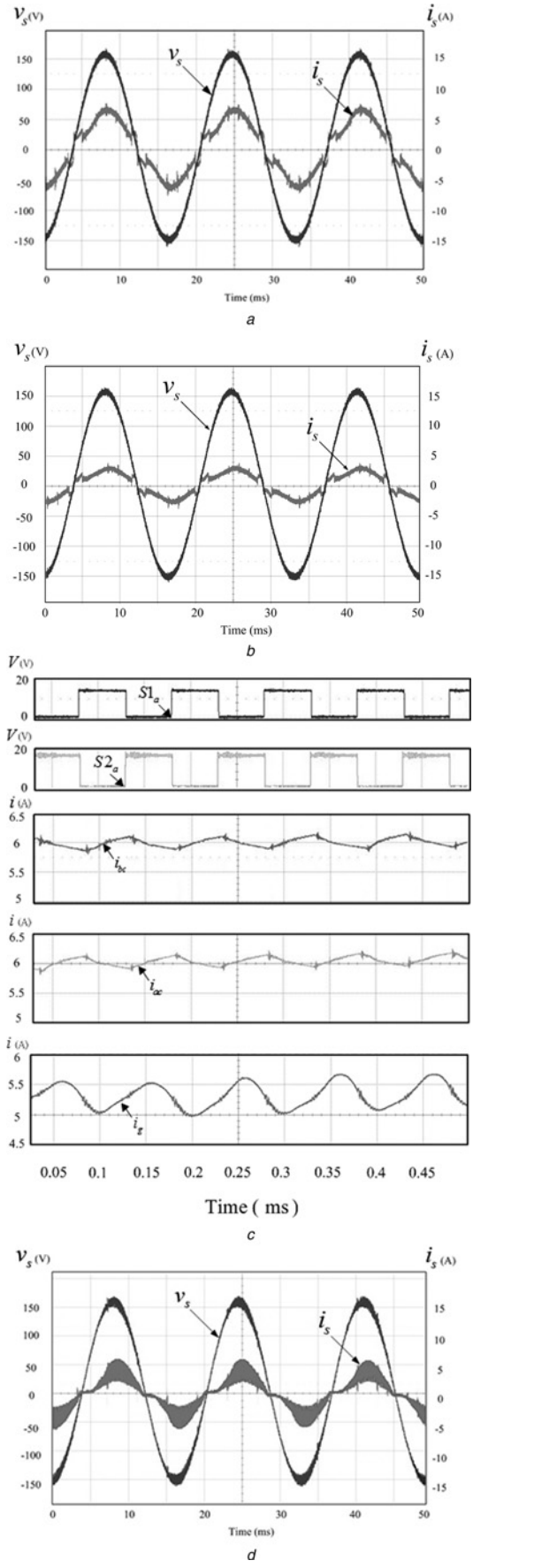

Fig. 9 *Measured input waveforms of the buck-converter charging*

a Constant current with interleave
b Constant voltage with interleave
c Switching states and current waveforms
d Constant current without interleave

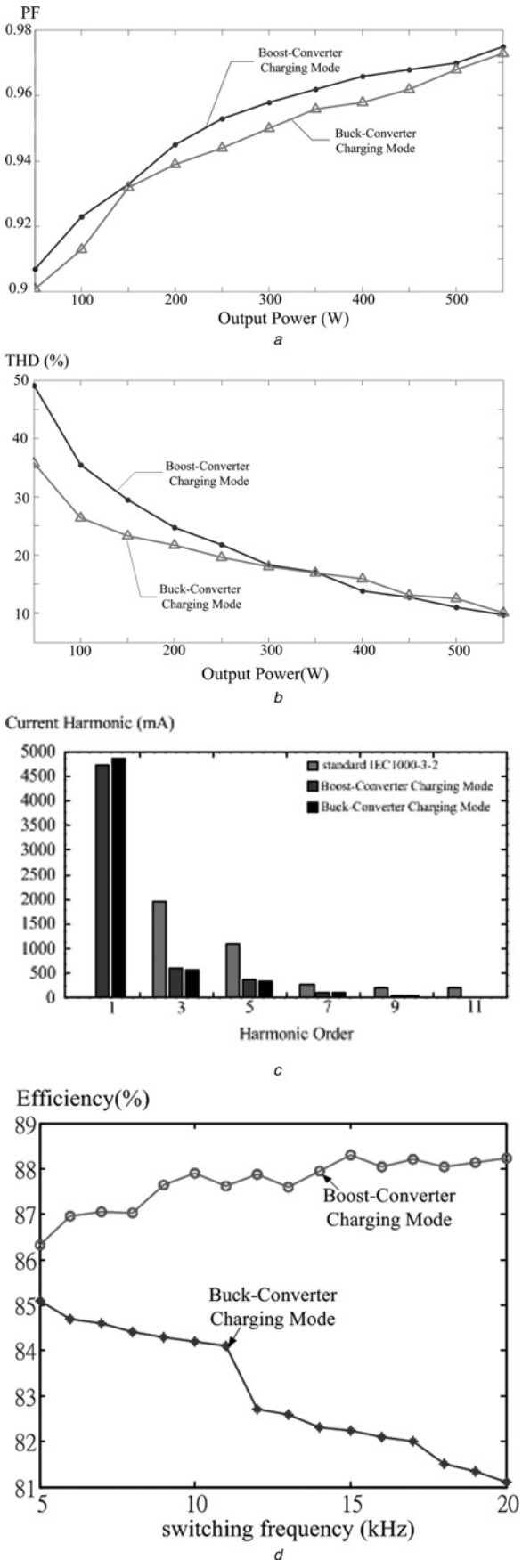

Fig. 10 *Measured results for power factor and harmonics*

a Power factor
b Total harmonic distortion
c Harmonics of low orders at 300 W
d Efficiency of the proposed charging system under different switching frequencies

doi: 10.1049/iet-epa.2014.0168

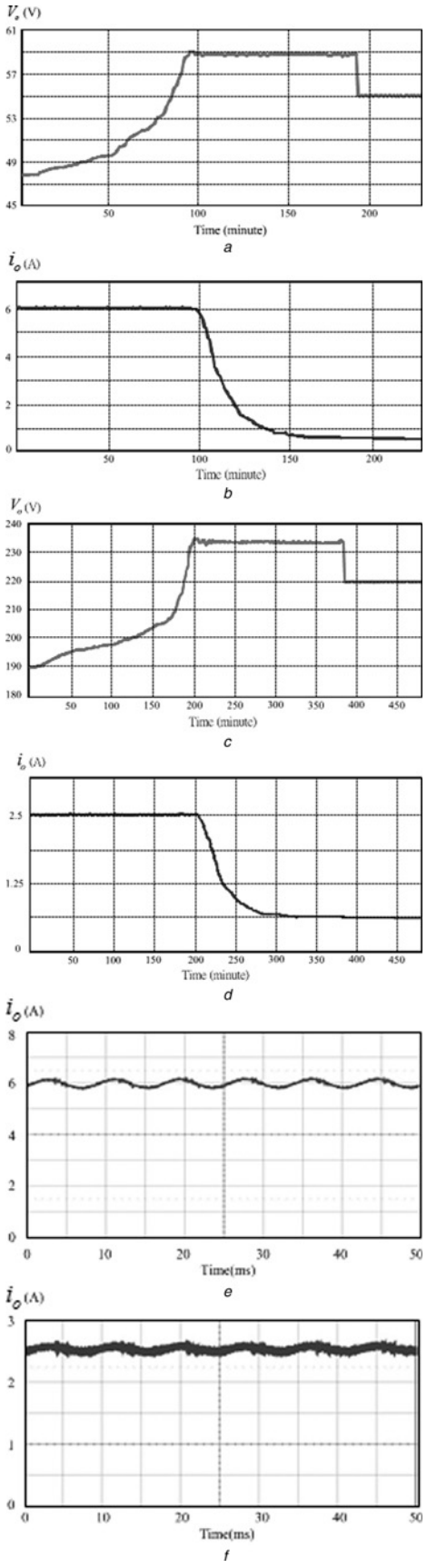

Fig. 11 *Measured waveforms of the battery set*

a Voltage using buck-converter
b Current using buck-converter
c Voltage using boost-converter
d Current using boost-converter
e Measured 6 A current waveform
f Measured 2.5 A current waveform

vice versa. The measured power factor of Fig. 9*c* is 0.9. As you can observe, the interleaving technique can cause the input current to become closer to a sinusoidal waveform because of the input filter. From Figs. 8*a*, *b* and 9*a*, *b*, we can conclude that the boost-converter charging mode has better performance than the buck-converter charging mode does.

Fig. 10*a* shows the relationship between the input power factor and the output power. Generally speaking, at the same output power, the boost-converter charging mode has a better power factor than the buck-converter charging mode does. In addition, the increase of the output power can improve the input power factor. Generally speaking, by using the proposed method, the measured input power factor varies from 0.9 to 0.97 when the output power changes from 0 to 550 W. Fig. 10*b* shows the measured results of the percentage of the total harmonic distortion.

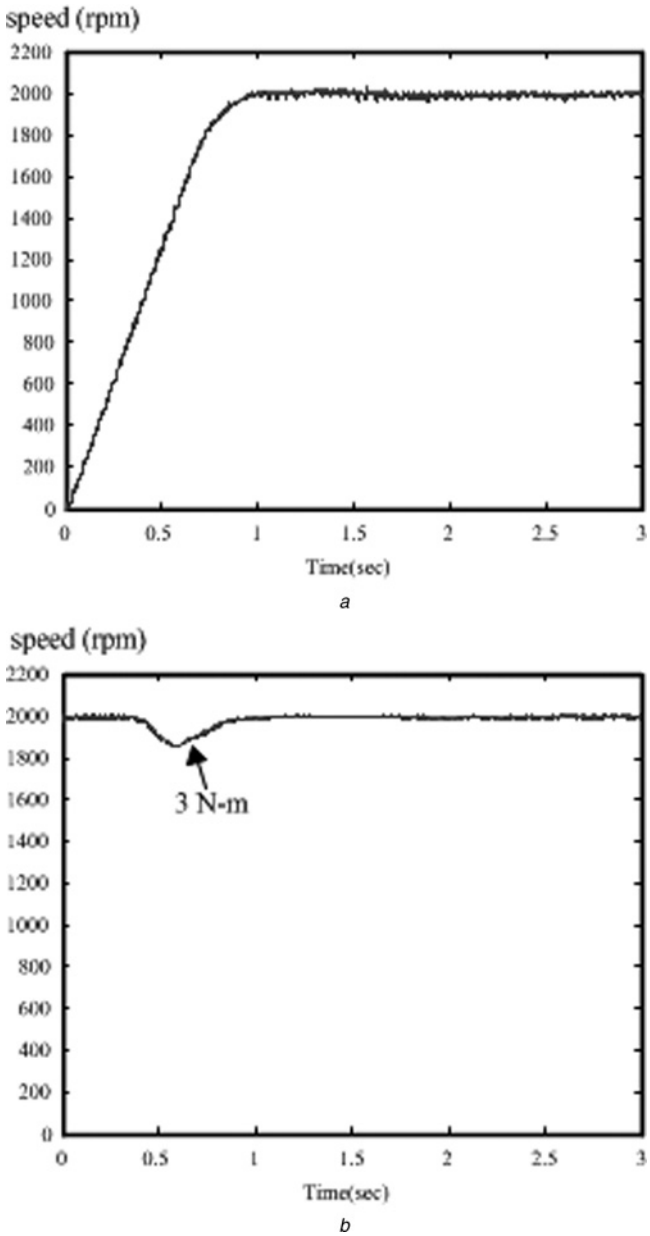

Fig. 12 Measured speed responses of the electric-propulsion system

a Transient response
b Load disturbance response

The total current harmonic distortion varies from 50 to 10% for the boost-converter charging mode; however, it varies from 36 to 10% for the buck-converter charging mode. Fig. 10*c* shows the input current harmonics at 300 W. Both the buck-converter charging mode and boost-converter charging mode can meet the requirements of the IEC 1000-3-2 standard. Fig. 10*d* shows the efficiency of the proposed charging system under different switching frequencies.

Figs. 11*a* and *b* show the measured averaging voltage and current waveforms of the 48 V battery set. First, a constant-current 6 A is used to charge the battery set. When the battery reaches its 83% capacity, the constant-voltage charging mode is used. Finally, the floating-voltage charging is applied. Figs. 11*c* and *d* show the measured averaging voltage and current of the 192 V battery set. First, a 2.5A constant-current is used to charge the battery set. When the battery reaches its 83% capacity, the constant-voltage charging mode is used. Finally, the floating-voltage charging mode is applied. Figs. 11*e* and *f* show the measured current of the 6 and 2.5 A charging states. Fig. 12 shows the measured speed responses of the electric-propulsion system. Fig. 12*a* is the measured transient response and Fig. 12*b* is the measured load disturbance response.

Generally speaking, the stator inductances of a PMSM is larger than the required inductance of the buck or boost converter. As a result, the proposed method can be applied for any small or large PMSM, which is operated at a normal switching frequency near 10 kHz for an integrated battery charger.

5 Conclusions

In this paper, a new method for an integrated battery charger for an electric-propulsion system is proposed. The proposed system can improve the power factor of the AC input source when it is operated in boost-converter charging or buck-converter charging. A diode bridge, an LC filter near the AC source, and three relays are added when compared with the traditional electric-propulsion system. As a result, the cost and volume of the charging system can be effectively reduced. Detailed analysis of the topology is given. Experimental results validate the theoretical analysis. The proposed method can be easily used in electric-propulsion systems because of its simplicity and low cost.

6 Acknowledgment

This paper is supported by the National Science Council, R.O.C., under grant NSC 102-2221-E-011-038.

7 References

1 Rajashekara, K.: 'Present status and future trends in electric vehicle propulsion technologies', *IEEE J. Emerging Sel. Top. Power Electron.*, 2013, **1**, (1), pp. 3–10
2 Zhang, M., Yang, Y., Mi, C.C.: 'Analytical approach for the power management of blended-mode plug-in hybrid electric vehicles', *IEEE Trans. Veh. Technol.*, 2012, **61**, (4), pp. 1554–1566
3 Wirasingha, S.G., Emadi, A.: 'Classification and review of control strategies for plug-in hybrid electric vehicles', *IEEE Trans. Veh. Technol.*, 2011, **60**, (1), pp. 111–122
4 Emadi, A., Lee, Y.J., Rajashekara, K.: 'Power electronics and motor drives in electric, hybrid electric, and plug-in hybrid electric vehicles', *IEEE Trans. Ind. Electron.*, 2008, **55**, (6), pp. 2237–2245
5 Emadi, A., Williamson, S.S., Khaligh, A.: 'Power electronics intensive solutions for advanced electric, hybrid electric, and fuel cell vehicular power systems', *IEEE Trans. Power Electron.*, 2006, **21**, (3), pp. 567–577
6 Khaligh, A., Dusmez, S.: 'Comprehensive topological analysis of conductive and inductive charging solutions for plug-in electric vehicles', *IEEE Trans. Veh. Technol.*, 2012, **61**, (8), pp. 3475–3489
7 Sousa, L.De, Silvestre, B., Bouchez, B.: 'A combined multiphase electric drive and fast battery charger for electric vehicles'. Proc. IEEE VPPC, Lille, France, 2010
8 Bruyere, A., Sousa, L.De, Bouchez, B., Sandulescu, P., Kestelyn, X., Semail, E.: 'A multiphase traction/fast-battery-charger drive for electric or plug-in hybrid vehicles'. Proc. IEEE VPPC, Lille, France, 2010
9 Lacroix, S., Laboure, E., Hilairet, M.: 'An integrated fast battery charger for electric vehicle'. Proc. IEEE VPPC, Lille, France, 2010
10 Chang, H.C., Liaw, C.M.: 'Development of a compact switched-reluctance motor drive for EV propulsion with voltage-boosting and PFC charging capabilities', *IEEE Trans. Veh. Technol.*, 2009, **58**, (7), pp. 3198–3215
11 Solero, L.: 'Nonconventional on-board charger for electric vehicle propulsion batteries', *IEEE Trans. Veh. Technol.*, 2001, **50**, (1), pp. 144–149
12 Sousa, L. De., Bouchez, B.: 'Combined electric device for powering and charging', International Patent WO 2010/057892 A1, 2010
13 Yilmaz, M., Krein, P.T.: 'Review of battery charger topologies, charging power levels, and infrastructure for plug-in electric and hybrid vehicles', *IEEE Trans. Power Electron.*, 2013, **28**, (5), pp. 2151–2169
14 Yilmaz, M., Krein, P.T.: 'Review of the impact of vehicle-to-grid technologies on distribution systems and utility interfaces', *IEEE Trans. Power Electron.*, 2013, **28**, (12), pp. 5673–5689
15 Lee, Y.J., Khaligh, A., Enadi, A.: 'Advanced integrated bidirectional AC/DC and DC/DC converter for plug-in hybrid electric vehicles', *IEEE Trans. Veh. Technol.*, 2009, **58**, (8), pp. 3970–3980
16 Haghbin, S., Khan, K., Zhao, S., Alakula, M., Lundmark, S., Carlson, O.: 'An integrated 20 kW motor drive and isolated battery charger for plug-in vehicles', *IEEE Trans. Power Electron.*, 2013, **28**, (8), pp. 4013–4029
17 Haghbin, S., Lundmark, S., Alakula, M., Carlson, O.: 'Grid-connected integrated battery chargers in vehicle applications: review and new solution', *IEEE Trans. Ind. Electron.*, 2013, **60**, (2), pp. 459–473
18 Khan, M.A., Husain, I., Sozer, Y.: 'Integrated electric motor drive and power electronics for bidirectional power flow between the electric vehicle and DC or AC grid', *IEEE Trans. Power Electron.*, 2013, **28**, (12), pp. 5774–5783
19 Pellegrino, G., Armando, E., Guglielmi, P.: 'An integral battery charger with power factor correction for electric scooter', *IEEE Trans. Power Electron.*, 2010, **25**, (2), pp. 751–759
20 Hunter, P.M., Anbuky, A.H.: 'VRLA battery virtual reference electrode: battery float charge analysis', *IEEE Trans. Energy Convers.*, 2008, **23**, (3), pp. 879–886
21 Chuang, Y.C., Ke, Y.L., Chuang, H.S., Chang, S.Y.: 'Battery float charge technique using parallel-load resonant converter for discontinuous conduction operation', *IEEE Trans. Ind. Appl.*, 2012, **48**, (3), pp. 1070–1078

doi: 10.1049/iet-epa.2014.0168